Impurity Ion Transport by Filamentary Plasma Structures

Nuclear Materials and Energy 19 (2019) 473–478

Contents lists available at ScienceDirect

Nuclear Materials and Energy

journal homepage: www.elsevier.com/locate/nme

Impurity ion transport by filamentary plasma structures

Hiroki Hasegawa[a,b,*], Seiji Ishiguro[a,b]

[a] Department of Helical Plasma Research, National Institute for Fusion Science, National Institutes of Natural Sciences, Toki, Gifu 509-5292, Japan
[b] Department of Fusion Science, SOKENDAI (The Graduate University for Advanced Studies), Toki, Gifu 509-5292, Japan

ARTICLE INFO

Keywords:
Blob
Hole
Boundary layer transport
Impurity ion
Particle-in-cell simulation

ABSTRACT

We have studied the impurity ion transport by a filamentary plasma structure with the three-dimensional electrostatic particle-in-cell simulation. The effective diffusivity of the impurity ions transported by a filamentary plasma structure has been calculated from the simulation result. The sequence of simulations has revealed that the effective diffusivity of impurity ions has a positive correlation with the poloidal size of a filament and a slight inverse correlation with the ion temperature, and that the effective diffusivity becomes quite small in the heavy impurity ion mass case.

1. Introduction

In recent experiments of magnetic confinement devices, the intermittent filamentary coherent structures called "blob" or "hole" have been observed in the boundary layer plasmas [1–12]. Such structures are thought to provide the radial non-diffusive transport in the boundary layer plasmas. Motivated by such experiments, many theoretical studies and numerical studies regarding the filament dynamics have been conducted on the basis of two-dimensional reduced fluid models [13, 14]. Furthermore, some numerical works, in which three-dimensional fluid simulations were carried out or some kinetic effects are included, have been performed [15–22]. The size of such structures on the cross-section is thought to be in meso-scale in many situations. In such situations, the full kinetic dynamics should be considered. Therefore, we have developed the three-dimensional (3D) electrostatic particle-in-cell (PIC) simulation code called the "p3bd" code [23–25] in order to study the kinetic dynamics on the filament phenomena. With the 3D-PIC simulation, we have demonstrated the self-consistent current system and the temperature structure in a blob [26] and have revealed the kinetic effect on the blob propagation dynamics [27]. Furthermore, the 3D-PIC code has shown that the dipolar profile of impurity ion density in a filament on the cross-section arises from the polarization drift and that a filament transports impurity ions [28]. The observed effective radial diffusivities of the impurity ion transported by a filament are comparable to the Bohm diffusion coefficient, $D_B = T_e/16(eB)$. The impurity ion transport by a filament has been also studied by the two-dimensional interchange turbulence fluid simulation with the test impurity ion particle model [29]. Filaments in helical devices propagate in the direction opposite to that in the low-field side of tokamak devices because the helical coil is placed immediately outside the scrape-off layer (SOL) region in a chamber of helical device and because the direction of grad-B in the SOL region in a helical device is outward, that is, from core edge to first wall. Thus, the impurity ion transport by filaments might contribute to the difference of impurity transport property between tokamak and helical devices [30, 31]. In our previous studies [28, 29], however, the quantitative evaluation of the effect of filaments on total impurity ion transport has been insufficiently conducted. Thus, in this paper, we have investigated the dependence of the impurity ion transport by a filament on various parameters with the 3D-PIC simulation and have found the relation between the effective diffusivity and various parameters. If we obtain such correlations, we can estimate the effect of filaments on the total transport of impurity ions. In Section 2, the simulation method and configuration are discussed. In Section 3, we show the simulation results and present the observed correlations with various parameters. Finally, we summarize this work in Section 4.

2. Simulation method and configuration

In this section, we briefly show the simulation method and configuration. In this study, we investigated the impurity ion transport by the filamentary plasma structure by means of a three-dimensional electrostatic (the temporal evolution of the electric field is solved and the magnetic field is constant in time) PIC simulation code in which the full plasma particle (electron, ion, and impurity ion) dynamics (including the Larmor gyration motion) of all particles in a filamentary structure

* Corresponding author at: National Institute for Fusion Science, 322-6 Oroshi-cho, Toki, Gifu 509-5292, Japan.
E-mail address: hasegawa.hiroki@nifs.ac.jp (H. Hasegawa).

https://doi.org/10.1016/j.nme.2019.04.005
Received 13 August 2018; Received in revised form 22 March 2019; Accepted 4 April 2019
Available online 10 April 2019
2352-1791/

and background plasma are calculated in three-dimensional space and three-dimensional velocity coordinates with the equation of motion. The self-consistent electric field formed by the charge density that is produced from all particles is solved with Poisson's equation in the code [32]. In order to investigate some fundamental physical properties in the phenomenon, additional collision processes [33] and heat and particle sources are not included in the simulation.

In the 3D-PIC simulation, an ambient magnetic field is given to be parallel to the z-axis and the magnitude of the magnetic field is set as $B = 2L_x B_{Lx}/(3L_x - x)$, i.e., $\partial B/\partial x > 0$, where L_x is the system size in the x direction and B_{Lx} is the magnetic field strength at $x = L_x$. Such a configuration means that the $-x$, y, and z directions correspond to the radial, poloidal, and toroidal directions, respectively. In the y direction, the periodic boundary condition is adapted. At $x = 0$, $z = 0$, and L_z, the electric potential is set as $\phi = 0$ at all times and particles are absorbed. At $x = L_x$, particles are reflected and $\partial\phi/\partial x = 0$. A plasma blob or a hole is initially given as a cylindrical profile along the magnetic field between both edges in the z direction. The initial density profile of the blob or the hole in the poloidal cross-section is produced by the Gauss distribution with the radial and poloidal widths, δ_{bx} and δ_{by}. The initial impurity ion density n_{imp0} is given by

$$n_{imp0}(x, y) = \frac{n_{imp1}}{2}\left[1 - \tanh\left(\frac{x - x_s}{\Delta_s}\right)\right], \tag{1}$$

where n_{imp1} is the initial density amplitude of the impurity ion, x_s is the radial position of the boundary of the impurity ion region, and Δ_s is the width of the transition region. Eq. (1) indicates that the impurity ions mainly exist on the outer side ($x < x_s$). The detailed descriptions regarding the methodology for distributing simulation particles in the system can be found in Refs. [25] and [28].

The simulation parameters are as follows. The number of spatial cells in the simulation system is set as $N_x \times N_y \times N_z = 64 \times 128 \times 2048$ and the grid spacing is $\Delta_g \approx 0.5\rho_s$, where $\Delta_g = L_x/N_x = L_y/N_y = L_z/N_z$, ρ_s is defined as $\rho_s = c_s/\Omega_i$, c_s is the ion acoustic speed given by $c_s = \sqrt{T_e/m_i}$, Ω_i is the ion cyclotron frequency at $x = L_x$, T_e is the initial electron temperature, and m_i is the ion mass. The time step width is $\Omega_i\Delta t \approx 1.2 \times 10^{-3}$ (in the blob propagation simulations) or $\Omega_i\Delta t \approx 1.3 \times 10^{-3}$ (in the hole propagation simulations). The ion-to-electron mass ratio is $m_i/m_e = 100$. The charges are set as $-q_e = q_i = q_{imp} > 0$. The initial impurity-to-electron temperature ratio is $T_{imp}/T_e = 0.01$. The ambient magnetic field strength at $x = L_x$ is $\Omega_i/\omega_{pi} = 0.5$, where ω_{pi} is the ion plasma frequency of the background plasma at $x = L_x$. The initial electron density ratio of the blob to the background plasma is $n_{eb0}/n_{e0} = 2.7$ in the simulations of blob propagation. Also, the initial electron density ratio between the center of the hole and the background is $(n_{e0} - n_{eh0})/n_{e0} = 0.27$ in the simulations of hole propagation. Here, n_{eb0} and n_{eh0} are the initial electron density amplitude of the blob and that of the hole, respectively. The radial size of a filamentary structure is $\delta_{bx} \approx 2\rho_s$. The initial center positions of the blob and the hole are $(x_{b0}, y_{b0}) = (3L_x/4, L_y/2)$ and $(x_{h0}, y_{h0}) = (L_x/2, L_y/2)$, respectively. The initial ratio between impurity ion and background electron densities is given as $n_{imp1}/n_{e0} = 0.05$ because it is ~5% in experiments for studies of impurity transports (e.g., Ref. [30]). The radial position of the boundary of the impurity ion region and the width of the transition region are $x_s/L_x = 0.625$ and $\Delta_s/L_x = 0.125$, respectively.

From the configuration and the parameters shown above, it is found that filaments in the simulations are in the sheath-connected regime (C_s and C_i) shown in Refs. [13] and [34] because collisionless plasma is assumed. Also, in this study, δ_*, which is the particular filament width for the long distance propagation caused by the state where the inertial term, the driving term, and the dissipation term are comparable with each other [13], is given by $\delta_*/\rho_s \approx [L_z^2/(\rho_s L_x)]^{1/5} = 8$.

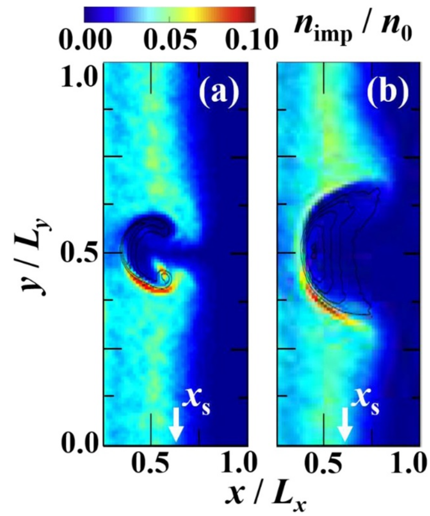

Fig. 1. Impurity ion density distributions on x-y plane at $z = L_z/2$ at the time when a blob penetrates the impurity ion region. In panel (a), the poloidal size of a blob is $\delta_{by}/\rho_s = 1.482$ and the time is $\Omega_i t = 90.1$. On the other hand, in panel (b), $\delta_{by}/\rho_s = 5.721$ and $\Omega_i t = 91.8$. Here, the initial ion temperature and the impurity ion mass are $T_i/T_e = 0.01$ and $m_{imp}/m_i = 4$, respectively. The black solid contour lines in each panel represent the electron density distributions.

3. Simulation results

3.1. Dependence on poloidal structure size

Fig. 1 shows the impurity ion density distributions on poloidal cross-section for $\delta_{by}/\rho_s = 1.482$ (a) and 5.721 (b) at the time when a blob penetrates the impurity ion region, where δ_{by} is the poloidal size of a filamentary structure. Also, Fig. 2 represents the impurity ion density distributions on poloidal cross-section for $\delta_{by}/\rho_s = 1.505$ (a) and 6.082 (b) at the time when a hole is moving from the impurity ion region to the region without impurity ions. As shown in Figs. 1 and 2, the impurity ions surrounding the blob and those in the hole are transported in the x direction. These figures indicate that the amount of the

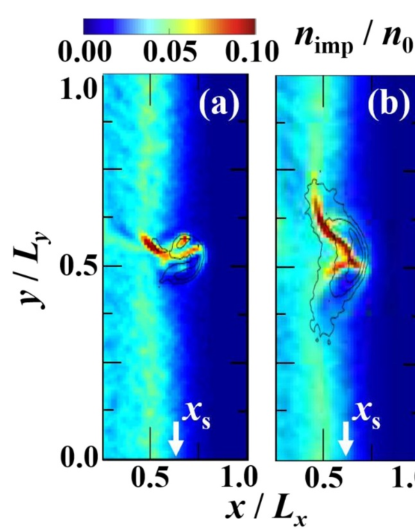

Fig. 2. Impurity ion density distributions on x-y plane at $z = L_z/2$ at the time when a hole is moving from the impurity ion region to the region without impurity ions. In panel (a), the poloidal size of a hole is $\delta_{by}/\rho_s = 1.505$ and the time is $\Omega_i t = 90.3$. On the other hand, in panel (b), $\delta_{by}/\rho_s = 6.082$ and $\Omega_i t = 91.2$. Here, the initial ion temperature and the impurity ion mass are $T_i/T_e = 0.01$ and $m_{imp}/m_i = 4$, respectively. The black solid contour lines in each panel represent the electron density distributions.

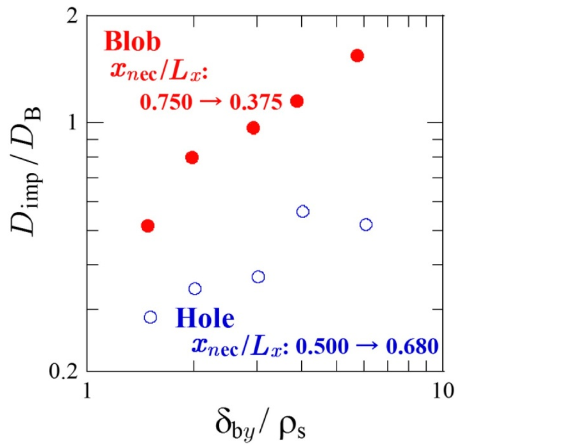

Fig. 3. Relation between the poloidal size of a structure and the observed effective diffusivity. The red closed circles and the blue open circles represent the observations in the blob propagation simulations and the hole propagation simulations, respectively. The observed effective diffusivity shown in this figure is the averaged diffusivity obtained by Eqs. (2) and (3). Here, x_{nec} is the electron center of mass of the filament.

impurity ions moving in the x direction over the boundary of the impurity ion region for $\delta_{by}/\rho_s \approx 6$ seems to be larger than the amount for $\delta_{by}/\rho_s \approx 1.5$.

In this study, in order to investigate quantitatively such a tendency mentioned above, the simulations for various poloidal sizes of a structure have been performed and the effective diffusion coefficient of the impurity ions at $x = x_s$ for each simulation has been obtained, where the effective diffusion coefficient is calculated by

$$D_{imp\perp} = \frac{\Gamma_{imp\perp}}{\nabla_\perp n_{imp}} = \frac{2\Delta_s \Gamma_{imp\perp}}{n_{imp1}}, \tag{2}$$

here, $\Gamma_{imp\perp}$ is the averaged impurity ion flux given by

$$\Gamma_{imp\perp} = \frac{1}{L_y L_z (t_1 - t_0)} \int_{t_0}^{t_1} \int_0^{L_z} \int_0^{L_y} \Gamma_{imp\perp}(x_s,\ y,\ z,\ t)\,\mathrm{d}y\,\mathrm{d}z\,\mathrm{d}t, \tag{3}$$

$\Gamma_{imp\perp}$ is the impurity ion flux in the x direction, t_0 and t_1 are the times when the center of electron mass in a blob is placed at $x/L_x = 0.75$ (which is the initial position) and $x/L_x = 0.375$. In the hole cases, t_0 and t_1 are times when the center of electron mass in a hole is placed at $x/L_x = 0.5$ (which is the initial position) and $x/L_x = 0.680$. In Fig. 3, the relation between the poloidal size of a structure and the observed effective diffusivity is shown. Here, some simulation parameters applied in these simulations are listed in Tables 1 and 2. Fig. 3 clearly reveals that the effective diffusivity has a positive correlation with the poloidal size.

3.2. Dependence on ion temperature

Fig. 4 shows the impurity ion density distributions on poloidal cross-section for $T_i/T_e = 0.01$ (a) and 1 (b) at the time when a blob penetrates the impurity ion region, where T_i is the initial temperature of the ion in background plasma and a filamentary structure. Also, Fig. 5 represents the impurity ion density distributions on poloidal cross-section for $T_i/T_e = 0.01$ (a) and 1 (b) at the time when a hole is moving from the

Table 1
Parameters of the blob simulations the results of which are shown in Section 3.1.

	Δ_g/ρ_s	$\Omega_i\Delta t$	δ_{bx}/ρ_s	δ_{by}/ρ_s
blob #1	0.4939	1.235×10^{-3}	1.975	1.482
blob #2	0.4919	1.230×10^{-3}	1.967	1.967
blob #3	0.4880	1.220×10^{-3}	1.952	2.928
blob #4	0.4841	1.210×10^{-3}	1.936	3.873
blob #5	0.4767	1.192×10^{-3}	1.907	5.721

Table 2
Parameters of the hole simulations the results of which are shown in Section 3.1.

	Δ_g/ρ_s	$\Omega_i\Delta t$	δ_{bx}/ρ_s	δ_{by}/ρ_s
hole #1	0.5017	1.254×10^{-3}	2.007	1.505
hole #2	0.5023	1.256×10^{-3}	2.009	2.009
hole #3	0.5034	1.258×10^{-3}	2.014	3.020
hole #4	0.5045	1.261×10^{-3}	2.018	4.036
hole #5	0.5069	1.267×10^{-3}	2.027	6.082

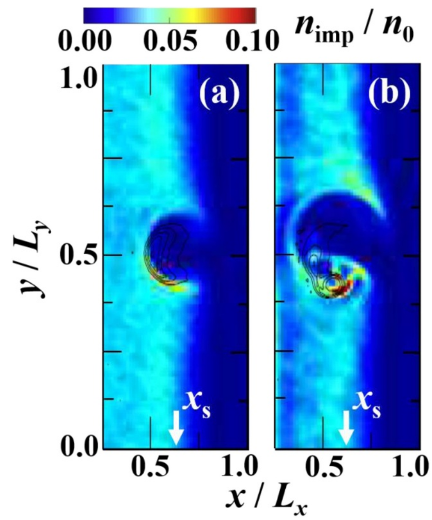

Fig. 4. Impurity ion density distributions on x-y plane at $z = L_z/2$ at the time $\Omega_i t = 56.6$ when a blob penetrates the impurity ion region. In panel (a), the initial ion temperature is $T_i/T_e = 0.01$. On the other hand, in panel (b), $T_i/T_e = 1$. Here, the poloidal size of a blob and the impurity ion mass are $\delta_{by}/\rho_s = 1.967$ and $m_{imp}/m_i = 4$, respectively. The black solid contour lines in each panel represent the electron density distributions.

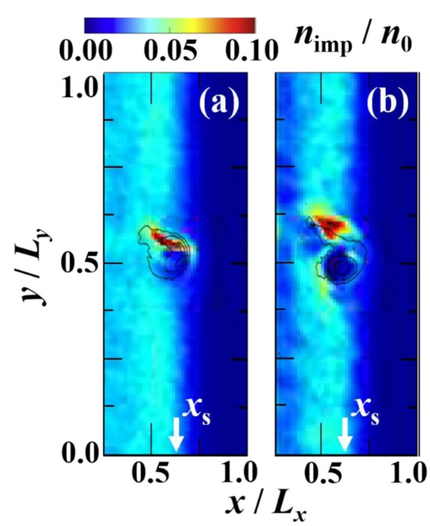

Fig. 5. Impurity ion density distributions on x-y plane at $z = L_z/2$ at the time $\Omega_i t = 57.8$ when a hole is moving from the impurity ion region to the region without impurity ions. In panel (a), the initial ion temperature is $T_i/T_e = 0.01$. On the other hand, in panel (b), $T_i/T_e = 1$. Here, the poloidal size of a hole and the impurity ion mass are $\delta_{by}/\rho_s = 2.009$ and $m_{imp}/m_i = 4$, respectively. The black solid contour lines in each panel represent the electron density distributions.

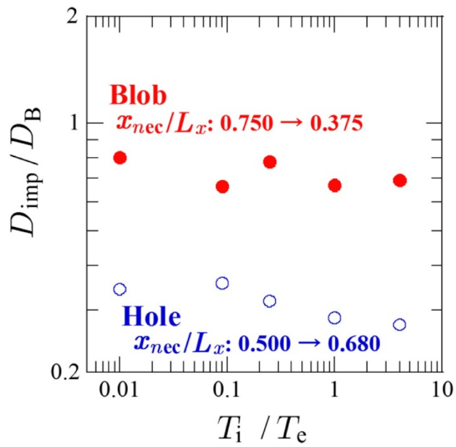

Fig. 6. Relation between the initial ion temperature and the observed effective diffusivity. The red closed circles and the blue open circles represent the observations in the blob propagation simulations and the hole propagation simulations, respectively. The observed effective diffusivity shown in this figure is the averaged diffusivity obtained by Eqs. (2) and (3).

impurity ion region to the region without impurity ions. As shown in Figs. 4 and 5, the poloidal symmetry breaking in the filament propagation occurs in the high ion temperature plasma [27], and such a poloidal asymmetry in the filament propagation influences the dynamics of impurity ions surrounding the blob or in the hole.

In order to estimate quantitatively such an effect of the poloidal asymmetry mentioned above, simulations for various ion temperatures have been performed and the effective diffusion coefficient of the impurity ions at $x = x_s$ for each simulation has been obtained. In Fig. 6, the relation between the ion temperature and the observed effective diffusivity is shown. Here, the parameters Δ_g, Δt, δ_{bx}, and δ_{by} are set as the same as those of “blob #2” shown in Table 1 or “hole #2” shown in Table 2. Fig. 6 reveals that the effective diffusivity has a slight inverse correlation with the ion temperature. This tendency is thought to arise from the poloidal asymmetry in the filament propagation in the higher ion temperature plasma. In high T_i cases, the dipole potential structure in a filament becomes asymmetric. That is, the potential hill in a filament becomes wider and lower, while the potential well becomes narrower and deeper [27]. Thus, the electric field around the potential well is enhanced, more impurity ions are trapped in the potential well, and more impurity ions rotate the potential well, i.e., some impurity ions move in the -x direction. Therefore, it is thought that the total impurity ion transport in the x direction is slightly reduced.

3.3. Dependence on impurity ion mass

Fig. 7 shows the impurity ion density distributions on poloidal cross-section for $m_{imp}/m_i = 2$ (a) and 40 (b) at the time when a blob penetrates the impurity ion region, where m_{imp} is the impurity ion mass. Also, Fig. 8 represents the impurity ion density distributions on poloidal cross-section for $m_{imp}/m_i = 2$ (a) and 40 (b) at the time when a hole is moving from the impurity ion region to the region without impurity ions. As shown in Figs. 7 and 8, the amount of the impurity ions which move around the blob in the x direction becomes larger in the light m_{imp} case than the amount in the heavy m_{imp} case. Also, the amount of the impurity ions which are trapped in the low potential side in the blob becomes larger in the heavy impurity ion case. Such a trapping is caused by the polarization drift, i.e., the simple acceleration by the electric field in a blob [28].

In order to investigate quantitatively the observed tendencies mentioned above, the simulations for various impurity ion masses have been performed and the effective diffusion coefficient of the impurity ions at $x = x_s$ for each simulation has been obtained. In Fig. 9, the

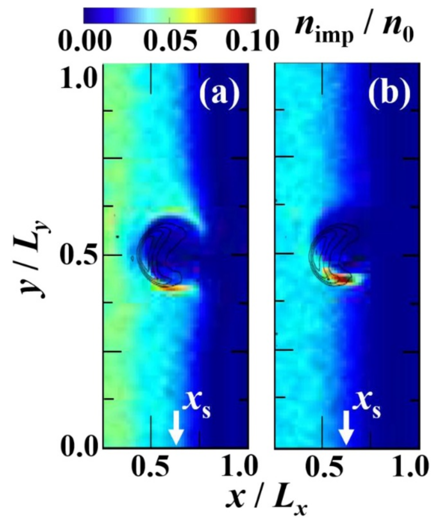

Fig. 7. Impurity ion density distributions on x-y plane at $z = L_z/2$ at the time $\Omega_i t = 63.9$ when a blob penetrates the impurity ion region. In panel (a), the impurity ion mass is $m_{imp}/m_i = 2$. On the other hand, in panel (b), $m_{imp}/m_i = 40$. Here, the poloidal size of a blob and the initial ion temperature are $\delta_{by}/\rho_s = 1.967$ and $T_i/T_e = 0.01$, respectively. The black solid contour lines in each panel represent the electron density distributions.

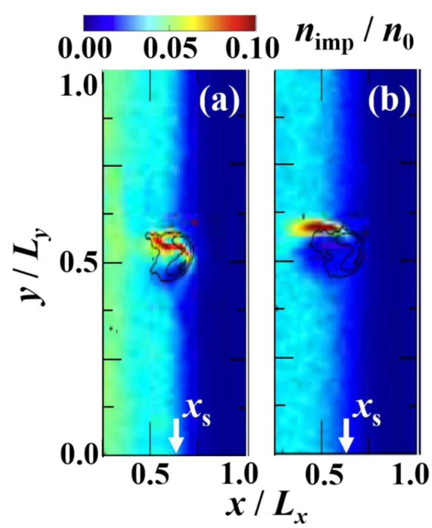

Fig. 8. Impurity ion density distributions on x-y plane at $z = L_z/2$ at the time $\Omega_i t = 65.3$ when a hole is moving from the impurity ion region to the region without impurity ions. In panel (a), the impurity ion mass is $m_{imp}/m_i = 2$. On the other hand, in panel (b), $m_{imp}/m_i = 40$. Here, the poloidal size of a blob and the initial ion temperature are $\delta_{by}/\rho_s = 2.009$ and $T_i/T_e = 0.01$, respectively. The black solid contour lines in each panel represent the electron density distributions.

relation between the ion temperature and the observed effective diffusivity is shown. Here, the parameters Δ_g, Δt, δ_{bx}, and δ_{by} are set as the same as those of “blob #2” shown in Table 1 or “hole #2” shown in Table 2. From Fig. 9, it is found that the effective diffusivity in the heaviest m_{imp} case has no longer a positive value. The reason for this is probably because the drift approximation of impurity ion motion is not available in the heavy m_{imp} case. That is, if the impurity ion motion is described by the drift approximation, the effective diffusivity has a certain positive value because the impurity ions are transported in the x direction by the $E \times B$ drift. However, if the impurity ion motion cannot be described by the drift approximation, the effective diffusivity becomes small because the impurity ions are not transported in the x direction but just move in the $\pm\ y$ direction due to the acceleration by

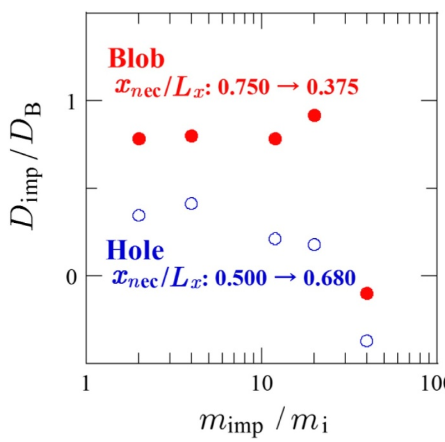

Fig. 9. Relation between the impurity ion mass and the observed effective diffusivity. The red closed circles and the blue open circles represent the observations in the blob propagation simulations and the hole propagation simulations, respectively. The observed effective diffusivity shown in this figure is the averaged diffusivity obtained by Eqs. (2) and (3).

the electric field in a filament. In actuality, t_1 which is described in Section 3.1 is $90 < \Omega_i t_1 < 150$ in these simulations. On the other hand, the time for one cyclotron motion of impurity ion is $\Omega_i t_{cimp} = 2\pi\ m_{imp}/m_i$. Thus, $t_{cimp} > t_1$ for $m_{imp}/m_i = 40$. That is, the impurity ion has not completed one cyclotron motion during the propagation in the heaviest m_{imp} case. Therefore, the impurity ions are difficult to transport by the $E \times B$ drift in the heavy m_{imp} case and the effective diffusivity for $m_{imp}/m_i = 40$ has no longer a positive value. Also, according to the above discussion, the value of the impurity ion mass threshold that divides the small transport and the large transport might be $14 < m_{imp}^{th}/m_i < 24$ in these cases.

4. Summary

In this paper, we have investigated the dependence of the impurity ion transport by a filament on various parameters with the 3D-PIC simulation. The sequence of simulations has revealed that the effective diffusivity of impurity ions transported by a filamentary structure has a positive correlation with the poloidal size and a slight inverse correlation with the ion temperature, and that the effective diffusivity becomes quite small in the heavy impurity ion mass case. These results suggest that the statistics regarding the size of filaments generated in devices are important for estimating the effect of filaments on the total impurity ion transport. Further, the impurity ion transport by filaments is not negligible in the high ion temperature plasma which is usually observed in the boundary layer plasmas. Furthermore, if the filament propagation time is sufficiently longer than the impurity ion gyration time, the impurity ion transport by filaments cannot be ignored. According to Eqs. (2) and (3) shown in Section 3.1, the effective diffusivity obtained in this study means the level of the impurity ion counter-radial transport per unit length in the poloidal direction. Therefore, if the filament production rate per unit length in the poloidal direction as the function of the filament poloidal size is found, the total transport in experiment will be estimated with the results obtained in this study.

In this work, we have evaluated the impurity ion transport by a filament with the effective diffusivity. However, since the filament transport is the convective, i.e., the non-diffusive phenomenon, the evaluation with the effective diffusivity might be insufficient to investigate the impurity ion transport by filaments. In future works, we will consider the method most appropriate to the evaluation and plan to investigate the contribution of filaments to the total impurity ion transport in boundary layer plasmas by comparing these simulation results with experiments. Also, we will confirm the impurity ion mass threshold described in Section 3.3 by the simulations for various impurity ion mass in near future and will consider the reason why the effective diffusivity is not positive small value but the negative value for $m_{imp}/m_i = 40$. Furthermore, if the blob regime mentioned in Section 2 varies with the change of the filament poloidal size, the impurity ion mass threshold also might be changed with the filament propagation speed. This issue is one of topics in future works.

Acknowledgments

The simulations were carried out on the “Plasma Simulator (PS)” (FUJITSU FX100) of NIFS and the high-performance computer system of Nagoya University. This work is performed with the support and under the auspices of the NIFS Collaboration Research programs (NIFS15KNSS058, NIFS17KNSS086, NIFS17KNXN342, NIFS17KNTS046, NIFS17KNTS049, and NIFS16KNTT038), supported by the NINS program of Promoting Research by Networking among Institutions (grant number 01421701), supported by a Grant-in-Aid for Scientific Research from Japan Society for the Promotion of Science (KAKENHI 23740411), and partially supported by “Joint Usage/Research Center for Interdisciplinary Large-scale Information Infrastructures” and “High Performance Computing Infrastructure” in Japan (Project ID: jh160023-NAH, jh170003-NAH, and jh180006-NAH).

References

[1] J.A. Boedo, D. Rudakov, R. Moyer, S. Krasheninnikov, D. Whyte, G. McKee, G. Tynan, M. Schaffer, P. Stangeby, P. West, S. Allen, T. Evans, R. Fonck, E. Hollmann, A. Leonard, A. Mahdavi, G. Porter, M. Tillack, G. Antar, Phys. Plasmas 8 (2001) 4826.
[2] G.Y. Antar, G. Counsell, Y. Yu, B. Labombard, P. Devynck, Phys. Plasmas 10 (2003) 419.
[3] R.J. Maqueda, G.A. Wurden, S. Zweben, L. Roquemore, H. Kugel, D. Johnson, S. Kaye, S. Sabbagh, R. Maingi, Rev. Sci. Instrum. 72 (2001) 931.
[4] J.A. Boedo, D.L. Rudakov, R.A. Moyer, G.R. McKee, R.J. Colchin, M.J. Schaffer, P.G. Stangeby, W.P. West, S.L. Allen, T.E. Evans, R.J. Fonck, E.M. Hollmann, S. Krasheninnikov, A.W. Leonard, W. Nevins, M.A. Mahdavi, G.D. Porter, G.R. Tynan, D.G. Whyte, X. Xu, Phys. Plasmas 10 (2003) 1670.
[5] H.Q. Liu, K. Hanada, N. Nishino, R. Ogata, M. Ishiguro, X. Gao, H. Zushi, K. Nakamura, A. Fujisawa, H. Idei, M. HasegawaQUEST Group, J. Nucl. Mater. 438 (2013) S513.
[6] G. Birkenmeier, P. Manz, D. Carralero, F.M. Laggner, G. Fuchert, K. Krieger, H. Maier, F. Reimold, K. Schmid, R. Dux, T. Pütterich, M. Willensdorfer, E. Wolfrumthe ASDEX Upgrade Team, Nucl. Fusion 55 (2015) 033018.
[7] S.J. Zweben1, J.R. Myra, W.M. Davis, D.A. D'Ippolito, T.K. Gray, S.M. Kaye, B.P. LeBlanc, R.J. Maqueda, D.A. Russell, D.P. Stotlerthe NSTX-U Team, Plasma Phys. Control. Fusion 58 (2016) 044007.
[8] S.Y. Allan, S. Elmore, G. Fishpool, B. Dudsonthe EUROFusion MST1 Team, the MAST Team, Plasma Phys. Control. Fusion 58 (2016) 045014.
[9] H. Tanaka, N. Ohno, Y. Tsuji, S. Kajita, S. Masuzaki, M. Kobayashi, T. Morisaki, H. Tsuchiya, A. Komorithe LHD Experimental Group, Phys. Plasmas 17 (2010) 102509.
[10] H. Tanaka, N. Ohno, Y. Tsuji, S. Kajita, S. Masuzaki, M. Kobayashi, T. Morisaki, A. Komorithe LHD Experimental Group, Plasma Fusion Res. 7 (2012) 1402152.
[11] E. De la Cal, P. Semwal, A.M. Aguilera, B. van Milligen, J.L. de Pablos, Z. Khan, C. Hidalgo, Plasma Phys. Control. Fusion 56 (2014) 105003.
[12] H. Tanaka, N. Ohno, Y. Tsuji, K. Okazaki, S. Kajita, Contrib. Plasma Phys. 52 (2012) 424.
[13] S.I. Krasheninnikov, D.A. D'Ippolito, J.R. Myra, J. Plasma Phys. 74 (2008) 679 and references therein.
[14] D.A. D'Ippolito, J.R. Myra, S.J. Zweben, Phys. Plasmas 18 (2011) 060501and references therein.
[15] F. Militello, N.R. Walkden, T. Farley, W.A. Gracias, J. Olsen, F. Riva, L. Easy, N. Fedorczak, I. Lupelli, J. Madsen, A.H. Nielsen, P. Ricci, P. Tamain, J. Young, Plasma Phys. Control. Fusion 58 (2016) 105002.
[16] D. Jovanović, P.K. Shukla, F. Pegoraro, Phys. Plasmas 15 (2008) 112305.
[17] J. Madsen, O.E. Garcia, J.S. Larsen, V. Naulin, A.H. Nielsen, J.J. Rasmussen, Phys. Plasmas 18 (2011) 112504.
[18] N. Bisai, P.K. Kaw, Phys. Plasmas 20 (2013) 042509.
[19] M. Wiesenberger, J. Madsen, A. Kendl, Phys. Plasmas 21 (2014) 092301.
[20] P. Manz, T.T. Ribeiro, B.D. Scott, G. Birkenmeier, D. Carralero, G. Fuchert, S.H. Müller, H.W. Müller, U. Stroth, E. Wolfrum, Phys. Plasmas 22 (2015) 022308.
[21] P.W. Gingell, S.C. Chapman, R.O. Dendy, C.S. Brady, Plasma Phys. Control. Fusion 54 (2012) 065005.
[22] R.M. Churchill, C.S. Chang, S. Ku, J. Dominski, Plasma Phys. Control. Fusion 59 (2017) 105014.
[23] S. Ishiguro, H. Hasegawa, J. Plasma Phys. 72 (2006) 1233.
[24] H. Hasegawa, S. Ishiguro, Plasma Fusion Res. 7 (2012) 2401060.
[25] H. Hasegawa, S. Ishiguro, Plasma Fusion Res 12 (2017) 1401044.

[26] H. Hasegawa, S. Ishiguro, Phys. Plasmas 22 (2015) 102113.
[27] H. Hasegawa, S. Ishiguro, Plasma 1 (2018) 61.
[28] H. Hasegawa, S. Ishiguro, Nucl. Fusion 57 (2017) 116008.
[29] T. Maeda, K. Tominaga, S. Yamoto, A. Hatayama, H. Hasegawa, S. Ishiguro, Contrib. Plasma Phys. 58 (2018) 505.
[30] M. Yoshinuma, K. Ida, M. Yokoyama, M. Osakabe, K. Nagaoka, S. Morita, M. Goto, N. Tamura, C. Suzuki, S. Yoshimura, H. Funaba, Y. Takeiri, K. Ikeda, K. Tsumori, O. Kanekothe LHD Experimental Group, Nucl. Fusion 49 (2009) 062002.
[31] Y. Nakamura, M. Kobayashi, S. Yoshimura, N. Tamura, M. Yoshinuma, K. Tanaka, C. Suzuki, B.J. Peterson, R. Sakamoto, T. Morisakithe LHD Experiment Group, Plasma Phys. Control. Fusion 56 (2014) 075014.
[32] C.K. Birdsall, A.B. Langdon, Plasma Physics via Computer Simulation, McGraw-Hill Book Company, New York, 1985.
[33] T. Pianpanit, S. Ishiguro, H. Hasegawa, Plasma Fusion Res. 11 (2016) 2403040.
[34] J.R. Myra, D.A. Russell, D.A. D'Ippolito, Phys. Plasmas 13 (2006) 112502.